Silicon nanopillar arrays with SiO_2 overlayer for biosensing application

B. Dev Choudhury,[1,*] R. Casquel,[2] M.J. Bañuls,[3] F.J. Sanza,[2] M.F. Laguna,[2] M. Holgado,[2] R. Puchades,[3] A. Maquieira,[3] C.A. Barrios,[4] and S. Anand[1]

[1]*School of Information and Communication Technology, KTH Royal Institute of Technology, Electrum 229, S-164 40 Kista, Sweden*

[2]*Centro Láser, Universidad Politécnica de Madrid, Campus Sur, 28031 Madrid, Spain*

[3]*Instituto de Reconocimiento Molecular, Departamento de Química, Universidad Politécnica de Valencia, Camino de Vera s/n, 46022 Valencia, Spain*

[4]*Instituto de Sistemas Optoelectrónicos y Microtecnología, Universidad Politécnica de Madrid, ETSI de Telecomunicación, CEI Moncloa,, 28040 Madrid, Spain*

**bikashdc@kth.se*

Abstract: We present the fabrication of silicon dioxide (SiO_2) coated silicon nanopillar array structures and demonstrate their application as sensitive optical biosensors. Colloidal lithography, plasma dry etching and deposition processes are used to fabricate SiO_2 coated Si nanopillar arrays with two different diameters and periods. Proof of concept bio recognition experiments are carried out with the bovine serum albumin (BSA)/antiBSA model system using Fourier transform visible and IR spectrometry (FT-VIS-IR) in reflection mode. A limit of detection (LoD) value of 5.2 ng/ml is estimated taking in to account the wavenumber uncertainty in the measurements.

OCIS codes: (040.6040) Silicon; (110.4235) Nanolithography; (180.3170) Interference microscopy; (220.4241) Nanostructure fabrication; (260.3160) Interference; (280.1415) Biological sensing and sensors; (280.4788) Optical sensing and sensors; (300.6300) Spectroscopy, Fourier transforms; (310.1860) Deposition and fabrication.

References and links

1. P. Holzmeister, G. P. Acuna, D. Grohmann, and P. Tinnefeld, "Breaking the concentration limit of optical single-molecule detection," Chem. Soc. Rev. **43**(4), 1014–1028 (2014).
2. H. Wang, X. Han, X. Ou, C. S. Lee, X. Zhang, and S. T. Lee, "Silicon nanowire based single-molecule SERS sensor," Nanoscale **5**(17), 8172–8176 (2013).
3. X. Fan, I. M. White, S. I. Shopova, H. Zhu, J. D. Suter, and Y. Sun, "Sensitive optical biosensors for unlabeled targets: A review," Anal. Chim. Acta **620**(1-2), 8–26 (2008).
4. H. S. Wasisto, S. Merzsch, A. Stranz, A. Waag, E. Uhde, T. Salthammer, and E. Peiner, "Silicon resonant nanopillar sensors for airborne titanium dioxide engineered nanoparticle mass detection," Sens. Actuators B Chem. **189**, 146–156 (2013).
5. A. M. Popa, B. Wenger, E. Scolan, G. Voirin, H. Heinzelmann, and R. Pugin, "Nanostructured waveguides for evanescent wave biosensors," Appl. Surf. Sci. **256**(3), S12–S17 (2009).
6. B. R. Murthy, J. K. K. Ng, E. S. Selamat, N. Balasubramanian, and W. T. Liu, "Silicon nanopillar substrates for enhancing signal intensity in DNA microarrays," Biosens. Bioelectron. **24**(4), 723–728 (2008).
7. J. K. Chen, G.-Y. Zhou, C. F. Huang, and F. H. Ko, "Using nanopillars of silicon oxide as a versatile platform for visualizing a selective immunosorbent," Appl. Phys. Lett. **102**(25), 251903 (2013).
8. Y. Nazirizadeh, F. Oertzen, K. Plewa, N. Barié, P. Jakobs, M. Guttmann, H. Leiste, and M. Gerken, "Sensitivity optimization of injection-molded photonic crystal slabs for biosensing applications," Opt. Mater. Express **3**(5), 556–565 (2013).
9. E. Stern, A. Vacic, N. K. Rajan, J. M. Criscione, J. Park, B. R. Ilic, D. J. Mooney, M. A. Reed, and T. M. Fahmy, "Label-free biomarker detection from whole blood," Nat. Nanotechnol. **5**(2), 138–142 (2010).
10. S. M. Wells, I. A. Merkulov, I. I. Kravchenko, N. V. Lavrik, and M. J. Sepaniak, "Silicon nanopillars for field-enhanced surface spectroscopy," ACS Nano **6**(4), 2948–2959 (2012).
11. R. J. Martín-Palma, M. Manso, and V. Torres-Costa, "Optical biosensors based on semiconductor nanostructures," Sensors (Basel) **9**(7), 5149–5172 (2009).
12. C. Xie, L. Hanson, Y. Cui, and B. Cui, "Vertical nanopillars for highly localized fluorescence imaging," Proc. Natl. Acad. Sci. U.S.A. **108**(10), 3894–3899 (2011).

13. M. Kandziolka, J. J. Charlton, I. I. Kravchenko, J. A. Bradshaw, I. A. Merkulov, M. J. Sepaniak, and N. V. Lavrik, "Silicon nanopillars as a platform for enhanced fluorescence analysis," Anal. Chem. **85**(19), 9031–9038 (2013).
14. V. Krivitsky, L. C. Hsiung, A. Lichtenstein, B. Brudnik, R. Kantaev, R. Elnathan, A. Pevzner, A. Khatchtourints, and F. Patolsky, "Si nanowires forest-based on-chip biomolecular filtering, separation and preconcentration devices: nanowires do it all," Nano Lett. **12**(9), 4748–4756 (2012).
15. K. Q. Peng and S. T. Lee, "Silicon nanowires for photovoltaic solar energy conversion," Adv. Mater. **23**(2), 198–215 (2011).
16. M. Altissimo, "E-beam lithography for micro-nanofabrication," Biomicrofluidics **4**(2), 026503 (2010).
17. C. M. Bruinink, M. Burresi, M. J. de Boer, F. B. Segerink, H. V. Jansen, E. Berenschot, D. N. Reinhoudt, J. Huskens, and L. Kuipers, "Nanoimprint lithography for nanophotonics in silicon," Nano Lett. **8**(9), 2872–2877 (2008).
18. M. Campbell, D. N. Sharp, M. T. Harrison, R. G. Denning, and A. J. Turberfield, "Fabrication of photonic crystals for the visible spectrum by holographic lithography," Nature **404**(6773), 53–56 (2000).
19. M. A. Wood, "Colloidal lithography and current fabrication techniques producing in-plane nanotopography for biological applications," J. R. Soc. Interface **4**(12), 1–17 (2007).
20. X. H. Li, P. F. Zhu, G. Y. Liu, J. Zhang, R. B. Song, Y. K. Ee, P. Kumnorkaew, J. F. Gilchrist, and N. Tansu, "Light extraction efficiency enhancement of III-nitride light-emitting diodes by using 2-D close-packed TiO2 microsphere arrays," J. Disp. Technol. **9**(5), 324–332 (2013).
21. G. Liu, H. Zhao, J. Zhang, J. H. Park, L. J. Mawst, and N. Tansu, "Selective area epitaxy of ultra-high density InGaN quantum dots by diblock copolymer lithography," Nanoscale Res. Lett. **6**(1), 342 (2011).
22. B. Dev Choudhury, A. Abedin, A. Dev, R. Sanatinia, and S. Anand, "Silicon micro-structure and ZnO nanowire hierarchical assortments for light management," Opt. Mater. Express **3**(8), 1039–1048 (2013).
23. H. V. Jansen, M. J. de Boer, S. Unnikrishnan, M. C. Louwerse, and M. C. Elwenspoek, "Black silicon method X: A review on high speed and selective plasma etching of silicon with profile control: an in-depth comparison between Bosch and cryostat DRIE processes as a roadmap to next generation equipment," J. Micromech. Microeng. **19**(3), 033001 (2009).
24. M. Holgado, C. A. Barrios, F. J. Ortega, F. J. Sanza, R. Casquel, M. F. Laguna, M. J. Bañuls, D. López-Romero, R. Puchades, and A. Maquieira, "Label-free biosensing by means of periodic lattices of high aspect ratio SU-8 nano-pillars," Biosens. Bioelectron. **25**(12), 2553–2558 (2010).
25. F. J. Sanza, M. Holgado, F. J. Ortega, R. Casquel, D. López-Romero, M. J. Bañuls, M. F. Laguna, C. A. Barrios, R. Puchades, and A. Maquieira, "Bio-photonic sensing cells over transparent substrates for anti-gestrinone antibodies biosensing," Biosens. Bioelectron. **26**(12), 4842–4847 (2011).
26. F. J. Ortega, M. J. Bañuls, F. J. Sanza, R. Casquel, M. F. Laguna, M. Holgado, D. López-Romero, C. A. Barrios, Á. Maquieira, and R. Puchades, "Biomolecular interaction analysis of gestrinone-anti-gestrinone using arrays of high aspect ratio SU-8 nanopillars," Biosensors **2**(4), 291–304 (2012).
27. M. K. Parka, J. S. Keea, J. Y. Quaha, V. Nettob, J. Songa, Q. Fanga, E. M. Fosseb, and G. Loa, "Label-free aptamer sensor based on silicon microring resonators," Sensors and Actuators B: Chem. **176**, 552–559 (2013).
28. R. D. Peterson, B. T. Cunningham, and J. E. Andrade, "A photonic crystal biosensor assay for ferritin utilizing iron-oxide nanoparticles," Biosens. Bioelectron. **56**, 320–327 (2014).

1. Introduction

In recent years there has been a strong demand for high sensitivity biosensors with detection limits down to single molecule levels [1–3]. For increasing the sensitivity of optical biosensors there have been several methods reported with different interrogation techniques [4,5], materials [6,7], and technologies [8,9]. Nanostructure based biosensors have been widely studied to achieve higher sensitivities. Semiconductor nanostructures in the form of nanopillars and nanowires have recently drawn increased attention due to their unique optical and structural properties [10]. Nanostructures have the advantage of higher surface to volume ratios that has been used in many practical applications including optical biosensing [11]. In the case of biosensing, nanopillars increase the effective area which can improve the sensitivity and the signal to noise ratio in the measurements. Vertical nanopillars have found several applications such as fluorescence imaging [12], field enhanced fluorescence analysis [13], and enhancing signal intensity in DNA microarrays [6]. With the well-established Si fabrication technology and superior material quality, nanostructured Si has been used in different applications including sensitive biosensors and photovoltaic cells [10], [13–15]. For top-down fabrication of silicon nanopillars, patterning and etching of the substrate is required. There are different patterning approaches such as e-beam lithography [16], nano imprint lithography [17], and holographic lithography [18], each with their own limitations and

advantages. Colloidal lithography is another technique to realize nanostructures, and involves relatively simple processing steps [19].

In this paper, we discuss the fabrication of silicon nanopillar arrays with a SiO_2 overlayer and describe their utilization for bio-recognition applications. A combination of colloidal lithography and plasma dry etching processes is used for nanopillar fabrication. Two sets of Si nanopillar arrays having two different periods are realized using self-assembled, hexagonally arranged, colloidal SiO_2 particles (diameter: 500 or 1000 nm) as etch masks. A conformal SiO_2 over-layer is deposited on the etched Si nanopillars by plasma enhanced chemical vapor deposition (PECVD). Optical interrogation with Fourier transform visible and IR (FT-VIS-IR) spectrometry is used to measure the spectral shifts in the reflection spectra of the nanopillar array due to changes in the effective refractive index caused by the attachment of biomolecules on the nanopillar surfaces. Biosensing responses of the nanopillar arrays are evaluated by monitoring the immobilization of BSA protein and the recognition of its specific antibody (anti-BSA). The SiO_2 over-layer is used to facilitate surface functionalization and provide the proteins a hydrophilic environment to prevent their denaturation.

2. Experimental

2.1 Fabrication of Si nanopillars with a SiO2 over-layer

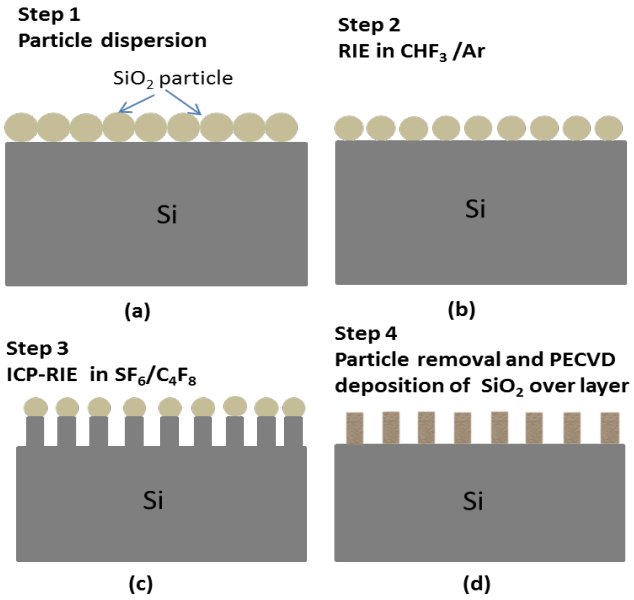

Fig. 1. (a)-(d): Schematics of SiO_2 coated Si nanopillar fabrication process steps. (a) SiO2 colloidal particles dispersed on a Si substrate. (b) Size reduction (by RIE) of the SiO_2 colloidal particles. (c) Anisotropic ICP-RIE etching of Si to produce Si nanopillars. (d) PECVD deposition of a SiO_2 over-layer on the Si nanopillars.

The fabrication process of Si nanopillars arrays consists of four steps, and include: 1) self–assembly of colloidal silica (SiO_2) spheres (colloidal lithography technique) on Si substrates, 2) size reduction of silica spheres by reactive ion etching (RIE), 3) Inductively coupled plasma reactive ion etching (ICP-RIE) of Si to etch nanopillar arrays, and 4) deposition of a SiO_2 over layer by PECVD. For etching high aspect nanopillars a pseudo Bosch process is used, wherein etching and sidewall passivation occur simultaneously, resulting in better side wall profiles. The process flow is schematically illustrated in Figs. 1(a)-1(d) and described in detail below.

Here, we have used single side polished Si (100) wafers cut in to 2 x 2 cm^2 pieces. These samples were first cleaned in organic solvents, dipped in 5% HF for 5 minutes to remove any native oxide on the surface, rinsed in DI water, and blow dried with nitrogen. The sample surfaces are made hydrophilic for better dispersion of the colloidal particles by treating them with O_2 plasma in a RF plasma chamber for 8 min; the RF power and the O_2 gas flow were 1000 W and 500 sccm, respectively. It is worth mentioning here that the plasma treatment time is optimized for 8 min to make the surface sufficiently hydrophilic to obtain monolayer coverage of silica particles in the subsequent dispersion step by spin coating.

A hexagonal close packed monolayer of silica particles is formed on the oxygen plasma treated samples by spin coating an aqueous suspension of SiO_2 particles (500 nm or 1000 nm in diameter). In the spin coating step, a solution dilution of 5% solids and spin speed of 1500 rpm for 30 s were found to be optimal to maximize the surface coverage of closely packed monolayer of silica particles. This procedure results in patches with monolayer coverage of silica particles, typically few mm^2 to a maximum of 1 cm^2 in area which are sufficient for the sensing experiments described here. However, uniform monolayer coverage of particles on a wafer scale is desirable for practical applications, and can be achieved using techniques such as rapid convective deposition [20] and diblock-copolymer lithography methods [21].

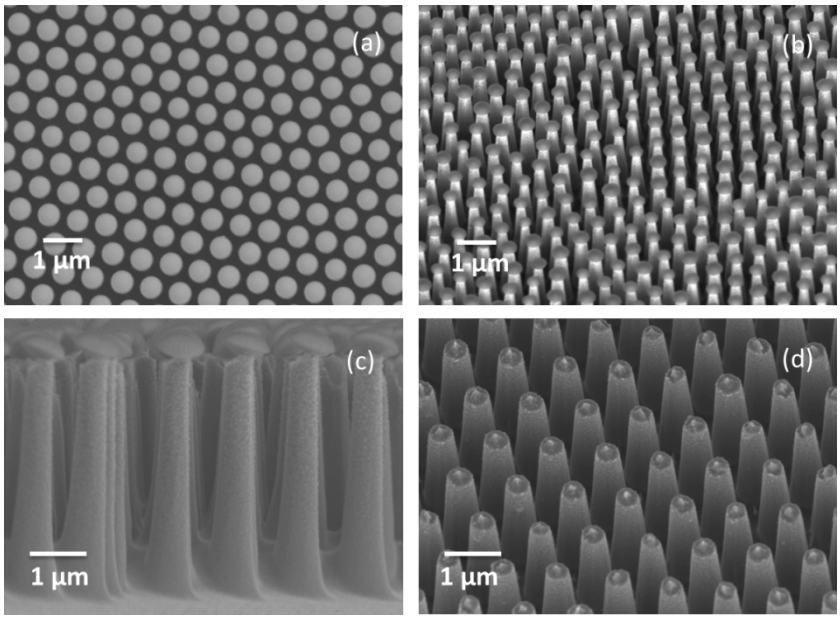

Fig. 2. Representative SEM images showing (a) an hexagonal array of colloidal SiO_2 particles on a Si sample, after size reduction by RIE; (b) a 20 degree tilted view of a 500 nm period Si nanopillar array with remnant silica (mask) particles; (c) cross sectional view of a 1000 nm period Si nanopillar array with remnant silica particles; and (d) a 20 degrees tilted view of a 1000 nm period nanopillar array.

The self-assembled hexagonally close-packed SiO_2 particles were size reduced and used as etch masks to fabricate Si nanopillar arrays with a period of 500 nm or 1000 nm depending on the particle diameter. The SiO_2 particles are size reduced by isotropic etching in a RIE chamber with Ar/CHF_3 chemistry. Etch durations of 5 and 10 min were used for reducing the 500 nm and 1000 nm silica particles, respectively. These were optimized for sufficient opening between the particles to facilitate subsequent etching of Si nanopillars. A representative scanning electron microscope (SEM) image of the self-assembled silica particles after size reduction by RIE is shown in Fig. 2(a). The diameter of and the spacing

between the etched pillars are predominantly determined by the silica (mask) particle size and the open space between the particles [22].

The Si nanopillars are fabricated in the 'pseudo Bosch' ICP-RIE method with SF_6 gas for etching and C_4F_8 gas for simultaneous surface passivation. This process is described in detail elsewhere [23]. In this work, C_4F_8 and SF_6 gas flows were kept at 90 and 35 sccm, respectively; and the chamber pressure at 10 mT. The RF platen and ICP powers are fixed at 10 and 575 W, respectively. The samples temperature is maintained at 20 °C by helium back-cooling. The Si samples with 500 nm and 1000 nm SiO_2 particles (masks) were etched for 8 and 16 min, to get two distinct sets of Si nanopillar arrays. The etch process results in a slightly tapered etch profiles and an etch rate of ~170 nm/min. After ICP-RIE, the SiO_2 mask particles are removed by placing the samples in 5% HF acid for 5 min. Figures 2(b)-2(d) show the SEM images of the fabricated Si nanopillar arrays having slightly tapered pillar profiles. Figure 2(b) shows a 20 degree tilted SEM image of a 500 nm Si nanopillar array sample fabricated using 500 nm SiO_2 particles as etch-masks; the nanopillar average height and diameter are 1600 and 200 nm, respectively. Figures 2(c) and 2(d) show cross sectional and 20 degrees tilted SEM images of the 1000 nm period Si nanopillar array samples fabricated using 1000 nm SiO_2 particles as etch-masks; the nanopillar average height and diameter are 3000 and 450 nm, respectively.

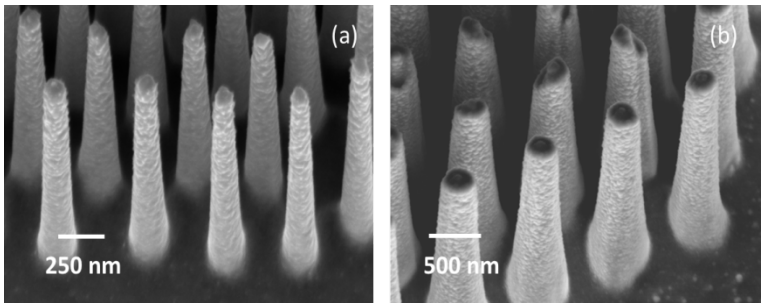

Fig. 3. SEM images (30 degree tilted views) of Si nanopillar arrays coated with a SiO_2 over-layer: (a) 500 nm period and (b) 1000 nm period.

Prior to coating the etched Si nanopillars with a SiO_2 over-layer, the samples are cleaned in organic solvents to remove any polymerized substances generated during the ICP-RIE step. For SiO_2 over-layer deposition we used the PECVD method in a 13.6 MHz capacitive RF plasma chamber. A ~100 nm thick SiO_2 layer was conformably deposited on the Si nanopillars with the following process parameters - gases: 2% SiH_4/N_2O (710 sccm) and N_2O (425 sccm); RF power: 20 W; pressure: 800 mT; temperature: 300 °C; and deposition time: 90 s. SEM images in Figs. 3(a) and 3(b) show both types of Si nanopillar arrays after conformal deposition of SiO_2 over-layer. Although the SiO_2 layer covers the etched nanopillar surfaces as desired, there could be thickness non-uniformity along the nanopillar sidewalls due to inherent limitations in the PECVD method combined with the nanopillar geometry (spacing, height and shape).

2.2 Sensing assay

For sensing assays, two sets of samples having two different pillar geometries were prepared by defining square sensing areas of 500 x 500 μm^2 by laser scribing (Nd:YVO4 solid state laser with a power of 1 W at a repetition rate of 15 KHz, emitting at 355 nm). Figure 4 shows the top view of one such sensing area. The two sets of samples are hereafter referred to as sample 'A' and 'B'. Sample A consists of tapered Si nanopillars with a thin SiO_2 over layer of 100 nm (approx.); pillar height~3000 nm, average diameter (averaged over the top and bottom diameters) ~ 450 nm and array period ~1000 nm. Sample 'B' consists of Si nanopillars with a ~100 nm SiO_2 over layer; nanopillar height ~1600 nm, average diameter

(averaged over the top and bottom diameters) ~200 nm and array period ~ 500 nm. Using the determined average nanopillar diameters and the periods (hexagonal lattice), the estimated "average" fill factors are 0.18 and 0.14 for samples A and B, respectively). The fill factor is calculated by considering an equilateral triangular lattice as unit cell. The sides of the triangle are equal to the period of the pillar arrays and consist of total half a circle having diameter equal to the average diameter of a pillar. We have also done a rigorous determination of available sensing surface areas of the two pillar samples, taking in to account the exact 3D structures. For sample A and sample B it results in 4.70 and 4.23 times higher sensing surface areas compared to normalized planar surface area.

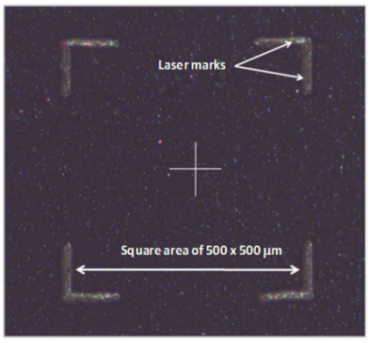

Fig. 4. Optical micrograph of a Si nanopillar sample showing a sensing area defined by laser scribing.

The sensing areas in the Si nanopillar array samples are optically characterized by measuring their spectral reflectance with a Vertex 70 Bruker Fourier transform near infrared interferometer [24–26]. Light focuses on the sample surface (Si nanopillar arrays) through a 15x Cassegrain objective, with an angle of incidence which varies from 15 to 22 degrees through a set of apertures. Spectral reflectance measurements are performed in the wavelength range of 400-1150 nm.

The BSA-anti-BSA model system is selected to test the bio-recognition capabilities of the Si-nanopillar samples. First, BSA protein is immobilized on the nanopillar surface by adsorption as follows: the samples were treated with piranha solution for 15 minutes (H_2SO_4/H_2O_2 3:1 v/v) at 50 °C; then they are incubated overnight in a PBS (phosphate buffered saline) solution of BSA (25 µg/ml) at room temperature in a humid chamber, washed with PBS and water, and dried. After BSA immobilization, the samples were incubated for 1 hour at room temperature at increasing concentrations of anti-BSA (0.1, 0.5, 1, 2.5, 5, 7, 10 and 20 µg/ml) in PBS. After each incubation step, the samples were washed with water and blow dried with N_2. The aforementioned BSA immobilization procedure and bio-recognition experiments with anti-BSA solutions were first tested and optimized on planar Si substrates coated with PECVD SiO_2, by a label-based assay characterization by developing with a biotinylated secondary antibody followed by gold labeled streptavidin and silver developer. Figure 5(a) shows an SEM image of sample 'A' after BSA treatment (functionalization) and Fig. 5(b) that of sample 'B' after BSA immobilization and anti-BSA bio-recognition assays.

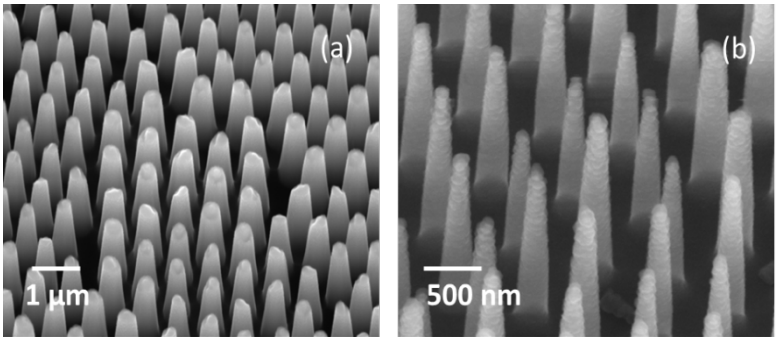

Fig. 5. SEM images of a) sample 'A' after BSA treatment (functionalization) and b) sample 'B' after BSA + anti-BSA biorecognition assays.

3. Results and discussion

Figure 6 shows the spectral reflectance curves of sample 'A' in Fig. 6(a) and 'sample B' in Fig. 6(b) before BSA functionalization. Reflectance differences in both magnitude and spectral features are observed between the two samples as expected from the different array properties and Si nanopillar heights. Reflectance maxima at 1030 nm (Sample 'A') and 1040 nm (Sample 'B') are attributed to constructive interferences produced by the air/nanopillar layer/substrate systems. Variations of the effective refractive index of the nanopillar layer due to the adhesion of molecules to the pillar surfaces should therefore lead to spectral shifts of such interference peaks (biosensor signal response). The range of the operating wavelengths is defined by the position of the interference maxima and minima. In the case of sample A, there are several dips and peaks in the reflectivity spectrum, whereas in sample B we only found one maxima at 1030 nm. We have chosen 1030nm and 1040nm wavelengths in order to compare the two samples. However, as the pillar diameter, height, shape and period can be controlled during fabrication albeit some process dependent limitations, the operating wavelength can also be selected within a range. Below we discuss 3D finite difference time domain (FDTD) simulations of the biosensor structures using commercial Lumerical FDTD simulation software.

The FDTD simulations were made taking to account the geometric parameters of the silica-coated Si nanopillars (Fig. 3), i.e. the period, size and shape. The pillars were assumed to be smooth and uniform, whereas in the actual samples the side-wall roughness and variations in shape and size of the pillars are present.

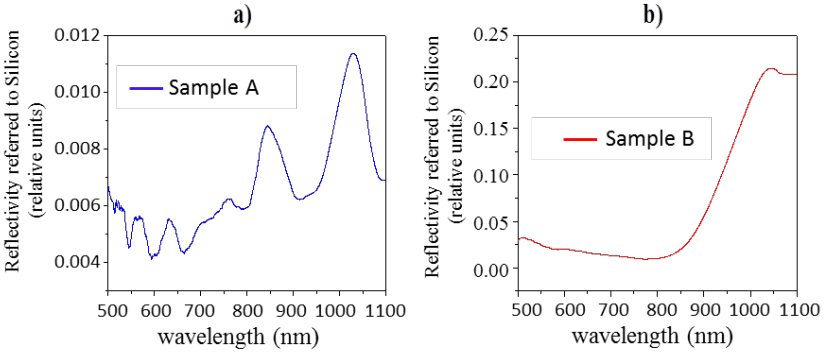

Fig. 6. Spectral reflectance curves of the Si nanopillar arrays obtained from the sensing areas in (a) sample 'A' and (b) sample 'B'.

As shown in Fig. 7(a), for sample A light is mainly confined inside the pillar; whereas in sample B significant portion of light is leaks outside the surface (Fig. 7(b)). The modal profiles shown in Fig. 7(a) and (b) are calculated for wavelengths at the resonance peak positions (Fig. 7(c) and 7(d)) for samples A and B, respectively. Since the refractive index change due to addition of biomolecules on the surface is a surface phenomenon, it is expected that the spectral shift for sample B is more than that in sample A. To evaluate the spectral shift due to biomolecules on the surface, we added a model bio-layer assuming a thickness of 20 nm and refractive index of 1.4 on the pillars in both sample A and B. The simulated total reflectivity spectra with and without the model bio-layer for samples A and B are shown in Fig. 7(c) and 7(d), respectively. We observe that the trends in the simulated reflectivity spectra are qualitatively consistent with the experimental data (Fig. 6). In addition, for sample B the shift in the reflection peaks around 1050 nm wavelength due to the model bio-layer is almost three times more than for sample A, which is qualitatively in compliance with the differences in optical field distribution in both types of pillars (Fig. 7 (a) and 7(b)).

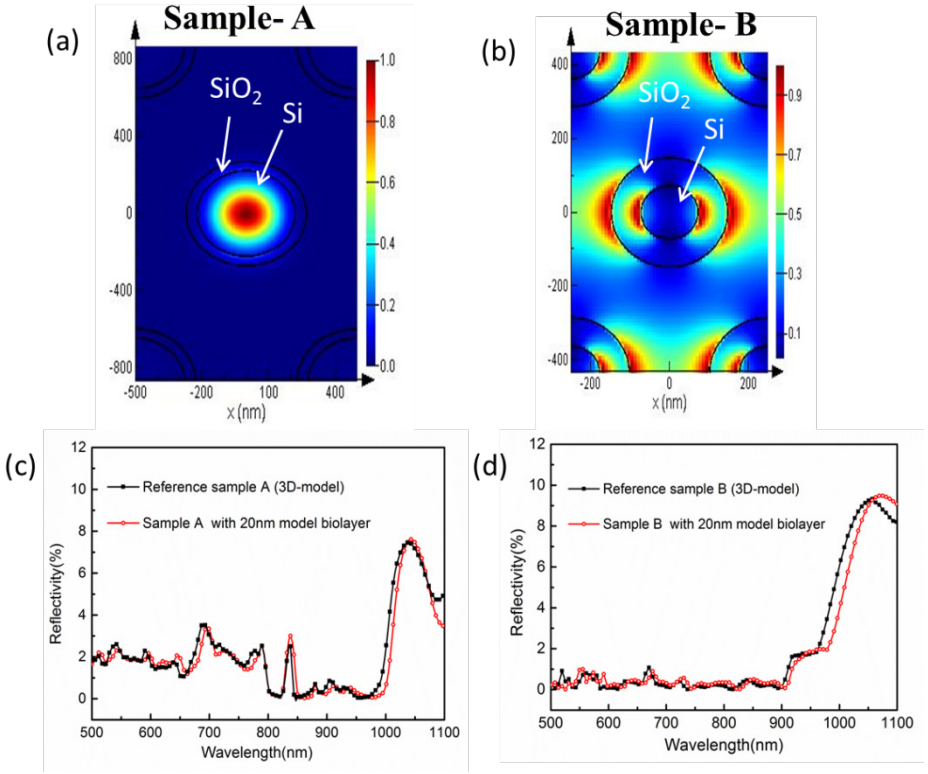

Fig. 7. (a) and (b) Axial cross section view at the middle of the pillar showing the field confinement in nanopillar array for sample A and sample B respectively. The color scale bar indicates the electric field intensity. (c) and (d) Reflection spectra showing the wavelength shift due to addition of the model bio-layer in sample A and sample B respectively.

Figures 8(a) and 8(b) show the spectral shifts of the aforementioned interference peaks as a function of anti-BSA concentration for sample 'A' and 'B', respectively. The reference and BSA saturation points are also included in the graphs, and indicate the spectral shifts between the reference (untreated) and BSA-treated samples, respectively. Both anti-BSA recognition curves show that at high anti-BSA concentrations signal saturation occurs as expected in a surface biosensing device. It is also seen that both the BSA and the anti-BSA saturation signals are higher for sample 'B' (BSA signal ≈1 nm for sample 'A' vs 2 nm for sample 'B';

anti-BSA saturation signal ≈1.3 nm for sample 'A' vs 5.7 nm for sample 'B'). This we attribute to the smaller nanopillar diameters (~200 nm) in sample B compared to that in sample A (~450 nm), and hence the optical modes could be more surface sensitive, which is also supported by the 3D FDTD simulations. However, we recognize that wettability could depend on the nanostructure geometry, and may also play a role in determining the surface coverage of biomolecules. This can also explain the larger experimental shift compared to simulated ones, as in the simulations we considered a conformal bio-layer for both samples A and B. More detailed studies by varying the nanopillar array geometries and further detail 3D electromagnetic simulations are necessary to optimize for best sensitivity.

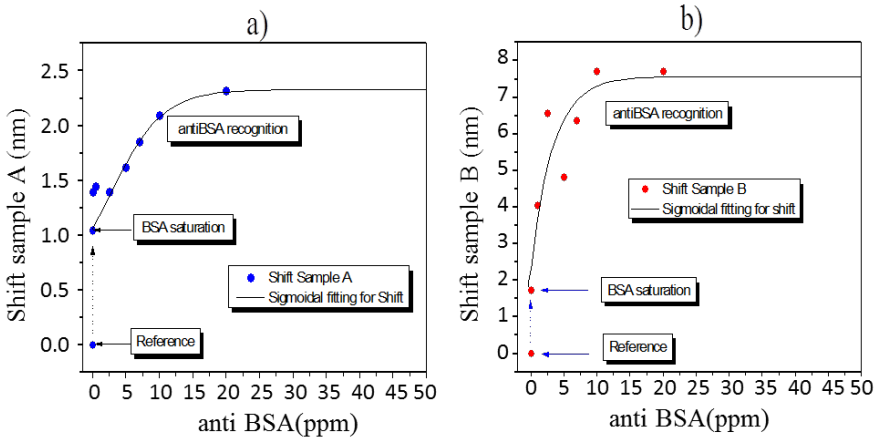

Fig. 8. Spectral shift of the interference peak versus anti-BSA concentration for (a) sample A (interference peak at 1030 nm) and (b) sample B (interference peak at 1040 nm); and the corresponding sigmoidal fits.

The limit of detection (LoD) for anti-BSA recognition is estimated considering the maximum slope ($m_{detection}$) of the sigmoidal fitting curves calculated with the experimental data; the resulting slopes ($m_{detection}$) are 0.123 nm/ppm and 1.2 nm/ppm for samples 'A' and 'B', respectively. The resolution of the spectrometer is 0.1 cm^{-1}, and the uncertainty in the measurement (u_w) can be calculated as $(u_w)^2 = (\text{Resolution})^2/12$ [24]. The expanded uncertainty (U_w) corresponding to a coverage probability of approximately 95% can be obtained by multiplying u_w by a coverage factor k = 2 (www.bipm.org, Evaluation of measurement data—guide to the expression of uncertainty in measurement (GUM)). With this data, U_w equals 0.00625 nm. LoD for anti-BSA recognition is calculated as $U_w/m_{detection}$, which results in 50.8 ng/ml and 5.2 ng/ml for Sample 'A' and Sample 'B', respectively. For the sake of comparison, the latter value is comparable to previous BSA-antiBSA experiments carried out with SU-8 nanopillar cells (2.3 ng/ml) [24], microring resonator biosensor (5.0 ng/ml) [27] and photonic crystal biosensor (26 ng/ml) [28]. Here we note that with FTIR one can obtain much better signal-to-noise ratio and resolution compared with other tools such as a conventional spectrometer. To have an order of magnitude estimate, if we choose an optical setup with a fiber focusing on the sample and a spectrometer with a resolution of 0.1 nm, the uncertainty of the measurements would be for this setup of $(u_w)^2 = (\text{Resolution})^2/12 = 0.029$ nm; with a coverage factor of 2 the expanded uncertainty is of 0.058 nm, resulting in a limit of detection value for sample 2 of 48.3ng/ml instead 5.2 ng/ml.

The results presented above demonstrate the suitability of the studied Si nanopillar array as a platform for highly sensitive biosensing, while offering relevant advantages over the aforementioned SU-8 nanopillars, such as: i) the possibility of including optoelectronic functionalities, such as photodetection, photocurrent (energy) generation, and current injection into the Si nanopillar layer; and ii) the use of cost-effective colloidal lithography,

instead of e-beam lithography used for SU-8 nanopillar fabrication, which favors mass production.

4. Conclusion

We have fabricated two sets of Si nanopillar arrays with two different periods and nanopillar diameters using colloidal lithography and dry etching. A SiO_2 overlayer is conformally deposited on the etched Si nanopillars. The two sets of Si/SiO_2 nanopillar structures on Si substrates have been evaluated as a platform for label-free optical biosensing based on interferometric reflectometry. The analyzed samples differ in nanopillar diameters and period, while having comparable filling factors. The BSA and anti-BSA model system has been used for immobilization/biorecognition testing. Both samples show an interference peak at around 1035 nm which has been used to monitor, by spectral shift measurements, the biomolecule attachment on the nanopillar surfaces. Both Si/SiO_2 -nanopillar structures show clear signal response to BSA immobilization and anti-BSA recognition tests, with the structure having the smaller nanopillar diameter exhibiting a higher sensitivity (5.2 ng/ml). While the Si nanopillar structures provide LoD values similar to those reported for SU-8 nanopillar arrays, they are potential advantages for optoelectronic integration and mass production. The sensing performance of these Si nanopillar arrays could be improved by (1) decreasing the filling factor (more separation among pillars and/or smaller pillar diameters) since this could increase wettability and the surface sensitivity of the optical modes; and 2) by increasing homogeneity and uniformity of the nanopillar array throughout the interrogation sample surface.

Acknowledgments

The authors from Sweden acknowledge support from the Linné center for advanced optics and photonics (ADOPT) funded by the Swedish Research Council(VR) and the EU-FP7 NoE Nanophotonics4Energy (N4E). The authors from Spain acknowledge support from the projects MASCREEN CTQ2010-15943 and PLATON TEC2012-31145 under the Spanish Ministry of Economy and competitiveness, and PROMETEO 2010/ 008 (Generalitat Valenciana).